Direct Calculations of One-, Two-, and Three-Dimensional Detonations by the CESE Method

Hao He[1], S.-T. John Yu[2]
Department of Mechanical Engineering
The Ohio State University,
Columbus, OH 43202
http://cfd.eng.ohio-state.edu/

Zeng-Chan Zhang[3]
Livermore Software Technology Corp.
Livermore, CA 94550
http://www.lstc.com/

Abstract

The present paper reports one-, two-, and three-dimensional numerical simulation of propagating detonations. We solve the Euler equations for chemically reacting flows with the space-time CESE method. The stiff source terms in the species equations are treated by a volumetric integration over a space-time region as an integral part of the space-time flux conservation. The classical ZND solution is used for code validation as well as the initial condition in the simulations. One-dimensional results include a piston problem and an instability problem. Two-dimensional cases include planar detonation waves and an oblique detonation over a ramp. Three-dimensional results include planar detonations in square ducts of various sizes. For H_2/air mixtures at various equivalence ratios, the cell size of the calculated soot trace compares well with experimental data. For the same flow conditions, the cell sizes of two-dimensional calculations are generally 30 to 40% less than that in three-dimensional ones. Moreover, both the amplitude and the frequency of the peak pressures in the calculated three-dimensional detonations are much higher than that in the two-dimensional results. Similarly, the frequency and amplitudes of the calculated two-dimensional pressure peaks are higher than that of the galloping one-dimensional detonations. While one- and two-dimensional simulations provide qualitative features of propagating detonations, one has to resort to three-dimensional simulations to obtain realistic flow structures of a detonation wave.

1. Introduction

Detonations are efficient processes of converting stored chemical energy in fuels to useful thermal and mechanical energy for various applications. In scramjet engines, standing detonation waves are the primary combustion mode and the associated blast waves also enhance fuel/air mixing. In pulsed detonation engines, the thrust power is directly from the high pressures behind detonations. Detonations were first recognized by Mallard and Le Chatelier. Chapman and Jouguet proposed the first theoretical model, which focuses on thermodynamic states before and after the detonation wave. The structure of a detonation wave was illustrated by Zeldovich, von Neumann, and Doering, i.e., the ZND model [1], in which a shock coupled with and followed by a combustion zone was depicted. Refer to Fig. 1. Further experiments, however, showed that detonation waves are unstable with transverse wave structure, and the unsteady pressure spikes are much higher than that predicted by the ZND model.

Recently, direct calculations of detonations have become quite commonplace [2-13]. Fickett and Wood [2] pioneered the numerical calculations of detonations by solving the one-dimensional Euler equations for reacting flows with the method of characteristics in conjunction with a shock fitting method. Longitudinal instability waves were accurately simulated. Taki and Fujiwara [3] reported the first two-dimensional simulation of detonations. They applied the upwind method for shock capturing and a two-step finite-rate model for modeling the ignition delay. Oran, Kailasanath, and coworkers [4-6] applied the FCT method to calculate detonations and reported detailed structures of two-dimensional detonations, including transverse waves, Mach stems, and fish-scale soot trace. Bourlioux and Majda [7] developed an accurate method, composed of a high-order upwind scheme, a front tracking method, and an adaptive refinement algorithm to calculate detonation waves. Papalexandris [8] developed an unsplit upwind method, which is based on integrating the flow equations along the characteristic manifolds in the space-time domain.

The first three-dimensional simulation of detonations was performed by Fujiwara and Reddy [9]. They studied detonation propagation in co-axial tubes. Williams et al. [10] reported the three-dimensional structure of detonations in a square channel. They reported the evolving incident waves and Mach stems in a rectangular pattern. By using the CESE method, direct calculations of three-dimensional detonations were reported by Zhang et al. [11, 12]. They reported the first simulated diagonal structure of propagating detonation in square tubes. Recently, Tsuboi et al. [13] also reported three-dimensional calculations of detonations by using a TVD scheme. They reported both rectangular and diagonal structures. In these three-dimensional calculations, the computational domains were very small and the discussions of the numerical results focused on the details of one or a handful of detonation cells.

[1] Ph.D. Candidate, AIAA Student Member, he.94@osu.edu.
[2] Associate Professor, AIAA Member, yu.274@osu.edu.
[3] Research Associate, AIAA Member.

In this paper, we report direct calculations of one-, two-, and three-dimensional detonations by using the space-time conservation element and solution element (CESE) method. Originally developed by Chang and coworkers, the CESE method [14-19] is a novel numerical framework for conservation laws. The CESE method employs a unified treatment for space and time to enforce local and global flux conservation. The objectives of the present paper are twofold. First, we wish to demonstrate the capability of the CESE method for calculating detonation waves. With a moderate mesh resolution, we will show that the CESE method is capable of capturing salient flow features of a propagating detonation wave in one-, two-, and three-dimensional calculations. Secondly, we will show that the structure of detonation waves is essentially three-dimensional and one has to conduct three-dimensional simulation to catch basic features of detonation waves, e.g., the cell size of the soot traces. We will clearly present the differences between the one-, two-, and three-dimensional results.

The rest of this paper is organized as follows. Section 2 provides a brief account of theoretical model. For completeness, the classical ZND analytical solution is summarized in an appendix. Section 3 illustrates the space-time CESE method. Section 4 reports numerical solutions. We then offer concluding remarks and provide cited references.

2. Model Equations

Model equations for chemically reacting flows with various levels of complexity exist. We have employed two approaches in the present paper. In the present section, we present the simpler one, which is consistent with the classical ZND model equations. Equation (2.1) shows the three-dimensional Euler equations for chemically reacting flows:

$$\frac{\partial u_m}{\partial t}+\frac{\partial f_m}{\partial x}+\frac{\partial g_m}{\partial y}+\frac{\partial q_m}{\partial z}=\mu_m\,, \qquad (2.1)$$

where m =1, 2, 3, 4, 5 and 6, indicating the continuity equation, the x-, the y-, and the z- momentum equations, the energy equation, and a species equation. In Eq. (2.1), the vectors are

$$[u_m]=\begin{pmatrix}\rho\\ \rho u\\ \rho v\\ \rho w\\ \rho E\\ \rho Z\end{pmatrix},[f_m]=\begin{pmatrix}\rho u\\ \rho u^2+p\\ \rho uv\\ \rho uw\\ (\rho E+p)u\\ \rho uZ\end{pmatrix},[g_m]=\begin{pmatrix}\rho v\\ \rho uv\\ \rho v^2+p\\ \rho vw\\ (\rho E+p)v\\ \rho vZ\end{pmatrix},$$

$$[q_m]=\begin{pmatrix}\rho w\\ \rho wu\\ \rho wv\\ \rho w^2+p\\ (\rho E+p)w\\ \rho wZ\end{pmatrix},\ [\mu_m]=\begin{pmatrix}0\\ 0\\ 0\\ 0\\ 0\\ \dot{\omega}\end{pmatrix}, \qquad (2.2)$$

where ρ is density; u, v, and w are three Cartesian velocity components; p is pressure; and Z is the mass fraction of the reactant. The total energy E is defined as

$$E=e+\frac{1}{2}(u^2+v^2+w^2)\,,$$
$$=\frac{p}{\rho(\gamma\text{-}1)}+Zq_0+\frac{1}{2}(u^2+v^2+w^2) \qquad (2.3)$$

where e is the specific internal energy, and q_0 is the heat of formation of the reactant. To close the equation set, the gas mixture is assumed polytropic, i.e., (i) the mole number of the reacting gas mixture is a constant; (ii) the molecular weight of the reacting gas mixture is a constant; (iii) the gas mixture is ideal, and (iv) the specific heats C_p and C_v of the gas mixture are constants. For ideal gases, $p = \rho RT$, where T is the temperature and $R = R_u/M_w$ is the gas constant. Note that R_u is the universal gas constant and M_w is the molecular weight of the gas mixture. To model chemical reactions, we consider a one-step irreversible reaction. The source term in the species equation, Eq. (2.2), due to chemical reaction is

$$\dot{\omega}=-K\exp(-E^+/R_uT)\,\rho Z\,, \qquad (2.4)$$

where K is reaction rate coefficient and E^+ is the activation energy.

To proceed, the above equations are made dimensionless based on the state of the unburned gas, i.e., ρ_0, p_0, T_0. A reference velocity is defined as $\sqrt{RT_0}$, which is in the same order of magnitude of the speed of the sound in the unburned gas. The reference length x_0 is chosen as the half- reaction length, $L_{1/2}$, which is defined as the distance between the detonation front and the point where half of the reactant is consumed by chemical reaction. The total energy E, the internal energy e, the heat release q_0 are made dimensionless by being divided by RT_0. The activation energy E^+ is non-dimensionalized by R_uT_0. The dimensionless variables are denoted by a bar on top each variable:

$$\overline{\rho}=\frac{\rho}{\rho_0}\,,\ \overline{p}=\frac{p}{p_0}\,,\ \overline{T}=\frac{T}{T_0}=\frac{\rho_0 RT}{p_0}\,,\ \overline{u}=\frac{u}{\sqrt{RT_0}}\,,$$
$$\overline{v}=\frac{v}{\sqrt{RT_0}}\,,\ \overline{w}=\frac{w}{\sqrt{RT_0}}\,,\ \overline{x}=\frac{x}{x_0}\,,\ \overline{t}=\frac{t}{x_0/\sqrt{RT_0}}\,,$$

$$\overline{K} = \frac{K}{\sqrt{RT_0}/x_0}, \quad \overline{E} = \frac{E}{RT_0}, \quad \overline{E}^+ = \frac{E^+}{R_u T_0}, \quad \overline{q}_0 = \frac{q_0}{RT_0}. \quad (2.5)$$

The form of the dimensionless governing equations remain unchanged except the source term,

$$\overline{\dot{\omega}} = -\overline{K}\overline{\rho}Z \exp(-\overline{E}^+/\overline{T}), \quad (2.6)$$

where the universal gas constant has been absorbed into the dimensionless activation energy. For convenience, the bar above each flow variable is dropped in the following discussions.

3. The Space-Time CESE Method

The CESE method, developed by Chang and coworkers [14-19] has been extensively illustrated in the cited references. In this paper, we present a brief discussion for solving the reacting Euler equations. Consider Eq. (2.1) and let $x_1 = x$, $x_2 = y$, $x_3 = z$, and $x_4 = t$ be the coordinates of a four-dimensional Euclidean space E_4. By using the Gauss divergence theorem, Eq. (2.1) becomes

$$\oint_{S(V)} \mathbf{h}_m \cdot d\mathbf{s} = \int_V \mu_m dV, \quad (3.1)$$

where $S(V)$ is the boundary of an arbitrary space-time region V in E_4, $d\mathbf{s}$ is a surface element vector pointing outward, and $\mathbf{h}_m = (f_m, g_m, q_m, u_m)$ is the space-time current density vector. Equation (3.1) states that the total space-time flux $\mathbf{h}_m$ leaving volume V through $S(V)$ must be balanced by the flux produced by the source term within V.

The CESE method integrates Eq. (3.1) in the space-time domain and solve for u_m in the new time levels. Contrast to the conventional finite volume methods, the CESE method has separate definitions of Conservation Element (CE) and Solution Element (SE). CEs are non-overlapping space-time domains such that (i) the whole computational domain can be filled by the union of all CEs; (ii) flux conservation is enforced over each CE or over a union of several neighboring CEs; and (iii) inside a CE, flow discontinuity is allowed. SEs are non-overlapping space-time domains such that (i) an SE does not generally coincide with a CE; (ii) the union of all SEs does not have to fill the whole computational domain; (iii) flow variables and fluxes are discontinuous across interfaces of neighboring SEs; and (iv) within a SE, flow variable and fluxes are assumed continuous, and they are approximated by the first-order Taylor series expansion in both space and time.

The time marching of the CESE method is based on a space-time staggered mesh such that the flow information propagates only in one direction across the interfaces of neighboring CE and towards the future. Refer to Fig. 3(a). Therefore, the integration of Eq. (3.1) is carried out without encountering a Riemann problem. In this paper, we use a modified space-time CESE method [17], which is an extension of the original CESE method. A single CE at each grid point is employed for solving conservation laws in one, two, and three spatial dimensions. Note that one has to use two CEs in one-dimensional, three CEs in two-dimensional, and four CEs in three-dimensional flows in the original CESE method. In what follows, we briefly discuss the modified CESE method in one, two, and three spatial dimensions.

3.1. One-Dimensional Euler Solver

Figure 3(b) shows the CE and the SE associated with grid point (j, n). The SE is composed of the rectangle $ABB'A'$ and the line segments QQ'' on the top of $ABB'A'$. The CE is rectangle $ABB'A'$. For any (x, t) within SE(j, n), $u_m(x, t)$ and $f_m(x, t)$ are discretized based on the first-order Taylor expansion and they are denoted by the superscript *:

$$u_m^*(x,t;j,n) = (u_m)_j^n + (u_{mx})_j^n (x - x_j) + (u_{mt})_j^n (t - t^n), \quad (3.2)$$

$$f_m^*(x,t;j,n) = (f_m)_j^n + (f_{mx})_j^n (x - x_j) + (f_{mt})_j^n (t - t^n). \quad (3.3)$$

Therefore,

$$\mathbf{h}_m^*(x,t;j,n) = (f_m^*(x,t,j,n), u_m^*(x,t,j,n)). \quad (3.4)$$

Equation (3.1) is approximated by the discrete form:

$$\oint_{S(CE)} \mathbf{h}_m^* \cdot d\mathbf{s} = \int_{CE} \mu_m dV \quad (3.5)$$

To integrate the right hand side, assume the source term μ_m is constant within SE(j, n). μ_m is evaluated based on the values of u_m at point (j, n). To evaluate the left-hand-side, we substitute Eqs. (3.2-4) into Eq. (3.5) and obtain

$$(u_m)_j^n - (\Delta t/2)(\mu_m)_j^n = [(u_m)_{j-1/2}^{n-1/2} + (u_m)_{j+1/2}^{n-1/2} + (s_m)_{j-1/2}^{n-1/2} - (s_m)_{j+1/2}^{n-1/2}]/2 \quad (3.6)$$

where

$$(s_m)_j^n = (\Delta x/4)(u_{mx})_j^n + (\Delta t/\Delta x)(f_m)_j^n + (\Delta t^2/4\Delta x)(f_{mt})_j^n. \quad (3.7)$$

Equations (3.6-7) are the algorithm for solving u_m. In Eq. (3.7), $(f_m)_j^n$ is a function of $(u_m)_j^n$, $(f_{mt})_j^n$ can be determined in terms of $(u_{mt})_j^n$ by chain rule, and $(u_{mt})_j^n$ can be obtained from Eq. (3.1) with no source term included:

$$(u_{mt})_{j\pm1/2}^{n-1/2} + (f_{mx})_{j\pm1/2}^{n-1/2} = 0, \quad (3.8)$$

where $(f_{mx})_j^n$ can be determined in terms of $(u_{mx})_j^n$ by chain rule. Owing to the source term on the left hand side, Eq. (3.6) is a nonlinear equation of $(u_m)_j^n$. Given the values of the marching variables at $t = t^{n-1/2}$, the right hand side of Eq. (3.6) can be explicitly calculated. $(u_m)_j^n$ is then solved by using Newton's iteration method. The initial condition for the iterations is calculated by using Eqs. (3.6-7) without the source term. To solve $(u_{mx})_j^n$ at point (n, j), central differencing is performed:

$$(u_{mx})_j^n = [(u_{mx}^+)_j^n + (u_{mx}^-)_j^n]/2, \quad (3.9)$$

where

$$(u_{mx}^{\pm})_j^n = \pm[(u_m)_{j\pm1/2}^n - (u_m)_j^n]/(\Delta x/2)\,, \tag{3.10}$$

$$(u_m)_{j\pm1/2}^n = (u_m)_{j\pm1/2}^{n-1/2} + (\Delta t/2)(u_{mt})_{j\pm1/2}^{n-1/2}\,. \tag{3.11}$$

For flows with discontinuities, Eq. (3.9) is further modified by a re-weighting procedure to add artificial damping:

$$(u_{mx})_j^n = W((u_{mx}^-)_j^n, (u_{mx}^+)_j^n, \alpha)\,, \tag{3.12}$$

where the function W is defined as

$$W(x_-, x_+, \alpha) = \frac{|x_+|^\alpha x_- + |x_-|^\alpha x_+}{|x_+|^\alpha + |x_-|^\alpha}\,. \tag{3.13}$$

α is an adjustable constant, and usually $\alpha = 1$ or 2.

3.2. Two- and Three-Dimensional Euler Solver

In two spatial dimensions, the computational domain is divided into non-overlapping quadrilaterals. Refer to Fig. 4(a). Vertices and centroids of quadrilaterals are marked by dots and circles, respectively. Q is the centroid of the quadrilateral $B_1B_2B_3B_4$. Points A_1, A_2, A_3, and A_4, respectively, are the centroids of the four neighboring quadrilaterals of the quadrilateral $B_1B_2B_3B_4$. Q^* marked by a cross in Fig. 4(a), is the centroid of the polygon $A_1B_1A_2B_2A_3B_3A_4B_4$. Point Q^*, which generally does not coincide with point Q, is referred to as the solution point associated with Q. Similarly, points A_1^*, A_2^*, A_3^*, and A_4^*, which are also marked by crosses, are the solution points associated with the centroids A_1, A_2, A_3, and A_4, respectively. To proceed, consider the space-time mesh shown in Fig. 4(b). Here $t = n\Delta t$ at the nth time level, where n = 0, 1/2, 1, 3/2, …. For a given n, Q, Q', and Q'', respectively, denote the points on the time levels n, n-1/2, and n+1/2 with point Q being their common spatial location. Other space-time mesh points in Fig. 4(b) are defined similarly.

To proceed, we discuss the geometry of CE and SE associated with Q^*. The numerical solution of the flow variables u_m at the nth time level are calculated based on the known flow solution in points at the previous time level n-1/2, denoted by superscript prime. To integrate Eq. (3.1), four Basic Conservation Elements (BCEs) of point Q^* are constructed, and they are denoted by BCE$_l(Q)$, with l = *1, 2, 3,* and *4*. These four BCEs are defined to be the space-time cylinders $A_1B_1QB_4A_1'B_1'Q'B_4'$, $A_2B_2QB_1A_2'B_2'Q'B_1'$, $A_3B_3QB_2A_3'B_3'Q'B_2'$, and $A_4B_4QB_3A_4'B_4'Q'B_3'$, respectively. The compounded conservation element of point Q, denoted by CE(Q), is defined to be the space-time cylinder $A_1B_1A_2B_2A_3B_3A_4B_4A_1'B_1'A_2'B_2'A_3'B_3'A_4'B_4'$, i.e., the union of the above four BCEs. Moreover, the SE of point Q^*, denoted by SE(Q^*), is defined as the union of CE(Q) and four plane segments $QQ''B_1''B_1$, $QQ''B_2''B_2$, $QQ''B_3''B_3$, and $QQ''B_4''B_4$.

With the definitions of the CE and SE, we proceed to illustrate the numerical integration of the space-time flux balance, i.e., Eq. (3.5). The flow variables and flux vectors, i.e., $u_m(x, y, t)$, $f_m(x, y, t)$, and $g_m(x, y, t)$, are approximated to their numerical counterparts, i.e., $u_m^*(x, y, t; Q^*)$, $f_m^*(x, y, t; Q^*)$, and $g_m^*(x, y, t; Q^*)$, based on the first-order Taylor series expansion with respect to $Q^*(x_{Q^*}, y_{Q^*}, t^n)$. As such, the space-time flux vector $\mathbf{h}_m(x, y, t)$, can be replaced by $\mathbf{h}_m^*(x, y, t; Q^*)$ and the numerical analogue of the space-time flux conservation is the same as Eq. (3.5) with an additional spatial dimension. By conducting the integration of Eq. (3.5) over the CE = BCE$_1$ + BCE$_2$ + BCE$_3$ + BCE$_4$, the discrete flow variables $(u_m)_{Q^*}$ associated with the space-time point Q^* can be straightforwardly evaluated. This is achieved by the aid of the geometrical information of CE(Q^*) as shown in Fig. 4(b), and the linear distribution of u_m in each SE by the first-order Taylor series expansion. Similar to that in the one-dimensional case, the source term μ_m is assumed constant in x and t within SE(Q^*) and it is evaluated based on the flow properties at Q^*. To solve the equations involving the stiff source term, Newton's method is used. The calculation of the gradient variables, i.e., $(u_{mx})_{Q^*}$ and $(u_{my})_{Q^*}$, is based on finite differencing with artificial damping, similar to that in the one-dimensional scheme.

To solve three-dimensional flow equations, the mesh is constituted of hexahedral cells. Refer to Fig. 4(c), where the symbols and letters are similar to that in Fig. 4(a). The hexahedron $B_1B_2B_3B_4B_5B_6B_7B_8$ is a cell located in the three-dimensional space with Q as its centroid. A_1 is the centroid of one of the six neighboring cells of $B_1B_2B_3B_4B_5B_6B_7B_8$. Point Q^* denotes the centroid of the 24-face polyhedron $B_1B_2B_3B_4B_5B_6B_7B_8A_1A_2A_3A_4A_5A_6$. The construction of CE and SE in the E_4 space is similar to that in E_3 for equations in two spatial dimensions. However, due to the complexity of the hyper planes and hyper cylinders in the four-dimensional space, the definition of the CE and SE is hard to be illustrated. For the complete description please refer to related papers [17]. The procedure of formulating the flux conservation and solving $(u_m)_{Q^*}$ and their spatial derivatives, i.e., $(u_{mx})_{Q^*}$, $(u_{my})_{Q^*}$, and $(u_{mz})_{Q^*}$, is a straightforward extension of that in two spatial dimensions, except more complex in geometry.

3.3. Non-Reflecting Boundary Conditions

Numerical treatments to achieve non-reflecting boundary condition in conventional CFD methods have been developed based on theorems of the partial differential equation, and they could be categorized into the following three groups: (i) applying the method of characteristics to the discretized equations, (ii) the use of the buffer zone or a perfectly matched layer, and (iii) applying asymptotic analytical solution at the far field. In the setting of the CESE method, we only concern the integral equation and the above ideas of treating non-reflective boundary are not applicable. Instead, the non-

reflecting boundary condition treatment here is based on flux conservation near the computational boundary and letting the flux from the interior domain to the boundary CE smoothly exit to the exterior of the domain. Because surface element of each CE allows flow information to be propagated into the future, the numerical implementation of this flux-based method is extremely simple. Chang and coworkers [18] have provided detailed discussions of various implementations of the above principle, including enforcing a back pressure.

4. Numerical Results and Discussions

4.1. One-Dimensional Detonations

Two one-dimensional detonation problems are considered: (i) a piston problem, which is initialized by pushing a piston into the reactant gas, and (ii) the instability problem, in which the analytical ZND solution is the initial condition and certain flow parameters are chosen to simulate the known flow instability phenomena.

We consider a long tube filled with the stagnant reactant gas. A piston on one end of the tube moves into the gas at a constant speed. We let the piston face as the origin of the spatial coordinate. In this coordinate system, the reactant gas charges into a closed-end tube at a constant speed. The reflected shock wave from the piston face raises the gas temperature and ignites the reactant. In the present study, the specific heat ratio $\gamma = 1.2$, the heat of formation $q_0 = 50$, and the activation energy $E^+ = 50$. Results of the linear-stability analysis [2] show that there is a critical overdriven factor f, below which the detonation is unstable. For the above parameters, the critical overdriven factor is $f^* = 1.72$. Two cases are considered: (i) a stable detonation with $f = 2$, and (ii) an unstable detonation at $f = 1.6$. For the stable case, the pressure history of shock front is shown in Fig. 5(a), in which the peak pressure of the established detonation wave remains constant after the initiation process. For the unstable case, Fig. 5(b) shows galloping pressures at the shock front when $t > 50$. Essentially, a longitudinal wave bounces back and forth, leading to pulsating peak pressures at the shock front. These results, including the values of the pulsating peak pressures and frequency of the instability wave, compare well with Fickett and Wood's results [2].

We then consider the instability problem. The analytical solution of an overdriven ZND wave is used as the initial condition. Again, two cases are calculated: (i) stable detonation with $f = 1.8$ and (ii) unstable detonation with $f = 1.6$. For the stable detonation $f = 1.8$, Fig. 6 shows the calculated p-v diagram as compared with the theoretical solution. The initial condition of $p = v = 1$ is located at the lower right corner of the figure. The solid line is the Hugoniot curves at various heat of formation q_0, and the dashed line is the Rayleigh line. The intersection of a Hugoniot curve and a Rayleigh line is the analytical solution of the final state of the detonation wave. Our CFD result is denoted by symbols of encircled cross. The analytical shock path, denoted by symbols of cross, is calculated by the analytical solution of the one-dimensional Navier-Stokes equations [20]. Chemical reactions and heat release occur along the Rayleigh line between the two Hugoniot curves of $q_0 = 0$ (the solution of the von Neumann spike) and $q_0 = 50$ (the final product). Across the jump condition of the shock front, there are two CFD solution points. The numerical solution shows that the artificial damping by the central differencing and the reweighing procedure in the CESE method produces flow solution very close to the real gas effects inside the shock wave predicted by the one-dimensional Navier Stokes equations.

Figure 7 shows the history of shock front pressures for an unstable detonation wave with $f = 1.6$, $\gamma = 1.2$, $q_0 = 50$, and $E^+ = 50$. The wave length of the oscillating pressures agrees well with that reported by Bourlioux and Majda [7]. To assess the numerical accuracy of the CESE method, the same calculation is repeated by using 5, 10, and 20 grid nodes to resolve the length of the half reaction zone. Figure 8 shows the peak pressures obtained by various upwind schemes as compared with the CESE method. The x axis in Fig. 8 is the relative mesh spacing, defined as $5/n$ with n as the number of mesh nodes for the half-reaction zone. According to Fickett and Wood [2], the maximum peak pressure with the above flow parameters is 98.6. As shown in Fig. 8, when 5 mesh nodes per half reaction zone is used, the CESE method produces a peak pressure about 98.2. When fine meshes are used, i.e., data points closer to the y axis, nuermcial results converge to 98.6.

4.2. Two-Dimensional Detonation Waves

We consider two cases in two-dimensional simulation of detonation waves: (i) an oblique detonation wave over a ramp, and (ii) planar detonation wave. For the first case, we consider the combustion of a supersonic premixed H_2-air flow over a ramp. The flow conditions were taken from previously reported works [21-23] as a standard test case for the NASP project in USA. In the present calculation, we adopt a two-step finite-rate chemistry model for H_2-air reaction, proposed by Korobeinikov et al. [24] and further developed by Taki and Fujiwara [3]. In this model, two species (a and b) equations are included in the equations set and the chemical reactions are split into two stages: (i) the induction period, leading to (ii) the exothermic process.

$$\frac{da}{dt} = \dot{\omega}_a = k_a \rho \exp\left(-\frac{E_a}{T}\right),$$

$$\frac{db}{dt} = \dot{\omega}_b = k_b P^2 \left[b^2 \exp\left(-\frac{E_b}{T}\right) - (1-b)^2 \exp\left(-\frac{E_b + Q/R}{T}\right)\right], \tag{4.1}$$

where a and b are the reaction progression parameters. The rate constants are chosen to correspond to the diluted oxygen-hydrogen mixture: $k_a = 0.3\times10^9$ m^3/(kg·s), $E_a =$

5000 K, $k_b = 0.1\times10^{-4}$ 1/(Pa^2·s), and $E_a = 2000$ K. Two inlet temperatures are considered: 900 K and 1200 K. The pressure of the free stream is 1 atm, and the Mach number is 4. The mixture ratio of the H_2/air gas is stochiometric. The angle of the ramp is 10^o. Figure 9 shows the flow solution of the 900 K case. The higher temperature and pressure behind the ramp shock ignite the reactant gas. Heat release due to the chemical reaction results in pressure increase, which causes the ramp shock to bend upward. In previously reported calculations [21-23], the calculated detonation wave was always an upward-bending smooth curve. Here we observe a distinct change of the shock angle and fine ripples travel back and forth along the detonation front. Emanating from the kink of the ramp shock, a shear layer propagates to the downstream. This instability was also reported in [22, 23]. Figure 10 shows the comparison of pressure and temperature between the present calculations and the previous results. The distributions of temperature and pressure are obtained from $y = 0.13$ cm above the bottom wall. Three earlier tests with different numerical schemes were considered, including an LU method [21], a PNS method [22], and a TVD scheme [23].

For the planar detonation wave, we consider a two-dimensional detonation wave propagating into a quiescent medium. The reaction zone is initialized by the analytical solution of the ZND wave with sinusoidal perturbations on the shock front. The flow parameters are $q_0 = 50$, $E^+ = 50$, $\gamma = 1.2$, and $f = 1.6$. The width of the computational domain is 7.5, and the height is 9.0 with the unit length as the half reaction zone. The flow conditions on the upper boundary surface are fixed according to the condition of the unburned gas. Periodic boundary condition is imposed at the two lateral boundaries. 54,000 quadrilateral cells are used for the computational domain.

Figure 11 shows the snapshots of the mass fraction, pressure, temperature, and vorticity. The flow field is much more complex than that of the one-dimensional detonations. The shock front is characterized by mushroom-shaped incident shocks interacting with Mach stems. The width of the Mach stem changes periodically due to the moving triple points at the shock front. At each collision of two triple points, a pair of vortices, with opposite rotational directions, are created and propagate downstream. Due to these vortices, unburned reactant is engulfed into the reaction zone and forms unburned pockets behind the reaction zone. The continuous burning of the unburned pockets shows the phenomena of explosions inside explosion and greatly extends the effective reaction zone.

4.3. Three-Dimensional Detonation Waves

In this section, we report three-dimensional simulations of planar detonations in square tubes. We will focus on the calculated cell size of the detonation soot trace, which is the most distinct flow feature of detonation waves. First, we consider a detonation wave in a square tube with cross section area comparable with the detonation cell size. Second, planar detonations in a duct with much larger cross section area are considered. For various flow conditions, including activation energies and heat release amount, we examine the corresponding changes in the calculated cell sizes. Finally, we will use the two-step induction chemistry model, Eq. (4.1), to calculate the averaged cell size of the soot trace cut on the side walls by the detonation waves. This result will be compared with the measured data. We will also compare the three-dimensional results with the results of the corresponding two-dimensional calculations.

In all three-dimensional calculations, the analytical solution with a small spatial perturbation on the shock front is employed as the initial condition. The detonation waves travel upwards to consume the fresh fuel/oxidant mixture. The upper boundary conditions are set to be the flow conditions of the unburned gas. The reflective wall boundary condition is used on the four lateral side walls. On the bottom surface, we impose the non-reflective boundary condition.

In a small duct with cross section of 8×8, we conduct three-dimensional simulation of a planar detonation wave. The length unit is the length of a half of the reaction zone. The numerical mesh is composed of about 6 millions hexahedral cells. The detonation parameters are $f = 1.6$, $\gamma = 1.2$, $E^+ = 50$, $q_0 = 50$. Figure 12 shows snapshots of the temperature contours and the contours of the mass fraction of the reactant. The side view of the three-dimensional contours resembles that of a two-dimensional detonation. The triple points in the two-dimensional detonations become triple lines and the interactions between the triple lines are much more complex than that in the two-dimensional calculations. The calculated three-dimensional flow structure is similar to that reported by Bauwens and coworkers [10].

We then consider detonation wave in a larger duct. The computational domain size is $40\times40\times40$, and is discretized by 9.6 million hexahedral cells. The detonation parameters are $\gamma = 1.2$, $q_0 = 50$, $E^+ = 50$, and $f = 1$. Figure 13(a) shows the calculated soot trace on one side wall. The soot trace is made visible by a continuous record of the shock front. The soot trace is the path of the triple points etched on the wall. Qualitatively, the structure of the calculated soot trace agrees well with the smoked foil records obtained in experiments [25].

To investigate the influence of detonation parameters on the cell size of the soot trace, we recalculate the same case with varied activation energies and heats of formation. Figure 13 shows results of this investigation. In general, larger q_0 results in larger cell size, and larger E^+ leads to smaller cell size. With E^+ decreased from 50 to 35, the cells become about three times larger.

To validate our three-dimensional calculation, we compare the calculated cell sized with the experimental data reported by Guirao et al. [26, 27]. In this calculation, Taki and Fujiwara's two-step induction model has been adopted. Figure 15 shows the calculated soot traces of the H_2/air detonation waves with four different equivalence ratios, i.e., Φ = 0.7, 0.8, 1.0, and 1.4. The cell widths are plotted in Fig. 16, including the case of Φ = 2. The result compared favorably with the experimental data [26, 27]. When the stochimetric fuel/air ratio is used, i.e., Φ = 1.0, the smallest cell size is obtained.

To further investigate the results, we conduct two-dimensional calculations for the case of Φ = 1.4 with identical flow conditions as that in the three-dimensional calculations. The numerical soot trace is shown in Fig. 17. Compared with its three-dimensional counterpart, i.e., Fig. 16(d), the averaged cell width in two-dimensional case is about 65% of that in the three-dimensional results. Similar calculations of two-dimensional detonations consistently show significantly smaller cell widths than that of the corresponding three-dimensional simulations.

Figure 18 shows the calculated time histories of the peak pressures at the shock front of a CJ detonation in a H_2/air mixture at Φ = 1.4. For the same flow condition, three sets of the results are plotted: (i) the ZND analytical solution, (ii) the two-dimensional CESE solution, and (iii) the three-dimensional CESE solution. The peak pressures of the two-dimensional detonation are about 2.5 times of that of the analytical solution because of continuously moving and colliding triple points at the shock front. For the same detonation wave, the maximum peak pressures by the three-dimensional simulation are markedly higher than that in the two-dimensional calculation. Moreover, the patterns and frequencies of the pressure fluctuations are distinctly different between the two- and the three-dimensional calculations. Two-dimensional results show a regular cyclical pattern with lower frequency, while the three-dimensional results are random with higher frequencies, because of much more complex three-dimensional structures.

5. Conclusions

In this paper, we have reported the one-, two- and three-dimensional simulations of detonation waves by using the space-time CESE method. In one-dimensional calculations, known features of steady detonations and unsteady detonations with a galloping pattern were successfully simulated. The results compared well with the results of classical stability analyses. The mesh refinement study showed that based on the use of the CESE method only 5 mesh nodes were needed to resolve a half of the reaction zone for accurate solutions. For two-dimensional calculations, we simulated oblique detonations in a supersonic H_2-air stream over a 10^o ramp. The pressure and temperature profiles along the ramp surface compared well with previously reported CFD results. For planar two-dimensional detonations, salient features have been crisply resolved, including transverse waves, triple points, Mach stems, counter rotating vortices, and unburned pockets inside the reaction zone. For three-dimensional calculations, the flow structure is very similar to that of the two-dimensional ones. However, further studies showed significance differences in key flow parameters between the two and three-dimensional simulations. For the same detonation wave, the averaged cell width of the two-dimensional result is about 30 to 40% smaller than that of the three-dimensional results. Moreover, both amplitudes and the frequencies of the pressure fluctuations at the shock fronts of the three-dimensional simulations are much higher than that of the two-dimensional simulations, which in turn, as repeatedly pointed out in the literature, are also significantly higher than that predicted by the classical one-dimensional ZND solution. Therefore, we conclude that one has to resort to three-dimensional calculations to catch the quantitative features of propagating detonation waves.

Appendix: The ZND Solution

Consider the one-dimensional Euler equations for chemically reacting gas flow:

$$\frac{\partial u_m}{\partial t} + \frac{\partial f_m}{\partial x} = \mu_m . \tag{A.1}$$

The employed species equation could be based on the combustion product instead of reactant, as stated in Section 2. Let λ = 1-Z be the mass fraction of the combustion product. When λ = 1, the chemical reaction is complete. Thus, λ is frequently referred to as the progress variable. In this case, the species equation changes to

$$\frac{\partial \rho\lambda}{\partial t} + \frac{\partial (\rho u\lambda)}{\partial x} = K\rho(1-\lambda)\exp\left(-\frac{E^+}{R_u T}\right) . \tag{A.2}$$

Accordingly, the internal energy becomes

$$E = e + \frac{u^2}{2} = \frac{pv}{\gamma - 1} - \lambda q_0 + \frac{u^2}{2} , \tag{A.3}$$

where $v=1/\rho$ is the specific volume.

Assume that the detonation wave propagates at a constant velocity D, and $\hat{u}$ = u-D is the velocity in the shock frame. By transforming the coordinates such that the spatial origin is fixed on the shock front, the equations of this steady problem in the new coordinate system become

$$d(\rho\hat{u})/dx = 0 , \tag{A.4a}$$

$$d(\rho\hat{u}^2 + p)/dx = 0 , \tag{A.4b}$$

$$d\left[(\rho E + p)\hat{u}\right]/dx = 0 , \tag{A.4c}$$

$$d(\rho\hat{u}\lambda)/dx = K\exp(-E^+/R_u T)\,\rho(1-\lambda) . \tag{A.4d}$$

For convenience, the carat on the top of velocity u is dropped hereafter.

Integrating the steady state continuity (A.4a), momentum (A.4b), and energy (A.4c) equations gives the classical Rankine-Hugoniot relations. The Rayleigh lines and Hugoniot curves on the *p*-*v* plane are described as follows, respectively:

$$u^2 = v^2 \frac{p - p_0}{v_0 - v}, \tag{A.5}$$

$$\frac{pv - p_0 v_0}{\gamma - 1} + \frac{1}{2}(p + p_o)(v - v_0) - \lambda q_0 = 0, \tag{A.6}$$

where the subscript '0' denotes the unburned state of the gas mixture, as introduced before, and the flow variables without subscript represents a flow condition other than the unburned condition, including inside the flame and the fully burned region.

After non-dimensionalization specified in Section 2, the unburned state can be described as

$$\rho_0 = p_0 = T_0 = 1,\ u_0 = \sqrt{\gamma} M_0,\ e_0 = \frac{1}{\gamma - 1}, \tag{A.7}$$

where M_0 is the Mach number of the unburned gas. And the equation of state changes to

$$pv = T. \tag{A.8}$$

By applying these dimensionless variables, the Rayleigh line and Hugoniot curve equations become

$$\gamma M_0^2 = (p - 1)/(1 - v), \tag{A.9}$$

$$\frac{pv - 1}{\gamma - 1} + \frac{(p + 1)(v - 1)}{2} - \lambda q_0 = 0. \tag{A.10}$$

Thus, the detonation/deflagration/shock solutions are the intersections of the Rayleigh lines and the Hugoniot curves. For convenience, the subscript "0" in M_0, which is a constant, is dropped.

By given values for the specific heat ratio γ, the Mach number of the unburned gas M, and the progressive variable λ, Eq. (A.9) and Eq. (A.10) are two equations for two unknowns, dimensionless specific volume v and pressure p, hence solvable. The solution gives

$$v = \frac{\gamma M^2 + 1}{M^2(\gamma + 1)}\left[1 \pm w\xi(\lambda)\right], \tag{A.11}$$

$$p = \frac{\gamma M^2 + 1}{\gamma + 1}\left[1 \mp \gamma w\xi(\lambda)\right], \tag{A.12}$$

where

$$w = \frac{M^2 - 1}{\gamma M^2 + 1},\ \xi(\lambda) = \sqrt{1 - \frac{q_0}{\Omega}\lambda}\ \text{, and}\ \Omega = \frac{\gamma(M^2 - 1)^2}{2(\gamma^2 - 1)M^2}. \tag{A.13}$$

The notation here follows that by Erpenbeck [28]. The temperature can be obtained readily by multiplying (A.11) to (A.12).

The above equations are the analytical solution of the classical R-H relations. Clearly, solution of thermodynamic variables p, v, and T are functions of the progressive variable λ only. Moreover, the two roots with positive and negative signs in Eq. (A.11) denote for the strong detonation solution and the weak detonation solution, respectively, between which located the upper Chapman-Jouguet point. Usually, the strong detonation solution is taken.

Based on the above discussions, all thermodynamic variables of the detonating gas mixture could be calculated as function of the combustion progressive variable λ. To proceed, consider the non-dimensionalized species equation at a steady state,

$$\frac{d\lambda}{dx} = \frac{K(1 - \lambda)}{u}\exp\left(-\frac{E^+}{T}\right). \tag{A.14}$$

By integrating the above equation with some numerical methods such as Runge-Kutta method, the spatial distribution of the mass fraction of the product species is obtained. With this information, spatial distribution in the reaction zone of all the thermodynamic variables, including pressure, specific volume, and temperature, can be determined. Then the value of the flow variables and the corresponding spatial derivatives are adopted as the initial condition for the dynamic detonation calculation. A typical ZND detonation wave solution, specified by the following flow parameters, is shown in Fig. 19: $\gamma = 1.2$, $q_0 = 50$, $E^+ = 50$, $f = 1.6$, where $f = D^2 / D_{CJ}^2$ is the overdriven factor. Because both flow variables and their spatial derivatives are used as the unknowns and solved simultaneously in the CESE method, the spatial derivatives of the flow variables are also required as part of the initial condition. This can be done by applying the chain rule to the correlative equations.

References

1. Fickett, W. and Davis, W. C., *Detonation*, University of California Press, Berkeley, California, 1979, pp. 13-15, 42-51.
2. Fickett, W. and Wood W. W., "Flow Calculations for Pulsating One-Dimensional Detonations," *Physics of Fluids,* Vol. 9**,** No. 3, 1966, pp. 903-916.
3. Taki, S. and Fujiwara, T., "Numerical Analysis of Two Dimensional Nonsteady Detonations," *AIAA Journal*, Vol. 16, No.1, 1978, pp. 73-77.
4. Oran, E., Young, T. and Boris, J., "Application of Time-Dependent Numerical Methods to the Description of Reactive Shocks," *Proceedings of the Combustion Institute*, Vol. 17, 1978, pp. 43-54.
5. Kailasanath, K., Oran, E. S., Boris, J. P., and Young, T. R., "Determination of Detonation Cell Size and the Role of Transverse Waves in Two-Dimensional Detonations," *Combustion and Flame*, Vol. 61, 1985, pp. 199-209.

6. Gamezo, V. N., Desbordes, D., and Oran, E. S., "Formation and Evolution of Two-dimensional Cellular Detonations," *Combustion and Flame*, Vol. 116, 1999, pp. 154-165.

7. Bourlioux, A. and Majda, A. J., "Theoretical and Numerical Structure of Unstable Detonations," *Philosophical Transactions of the Royal Society of London,* Series A, Vol. 350, 1995, pp. 29-68.

8. Papalexandris, M. V., "Unsplit Numerical Schemes for Hyperbolic Systems of Conservation Laws with Source Terms," Ph.D. Thesis, California Institute of Technology, 1997.

9. Fujiwara, T. and Reddy, K. V., "Propagation Mechanism of Detonation – Three-Dimensional Phenomena," *Memoirs of the School of Engineering, Nagoya University*, Vol. 41, No. 1, 1989, pp.93-111.

10. Williams, D. N., Bauwens, L., and Oran, E. S., "Detailed Structure and Propagation of Three-Dimensional Detonations," *Proceedings of the Combustion Institute*, Vol. 26, 1996, pp. 2991-2998.

11. Zhang, Z. C., Yu, S. T. J., He, H., and Chang, S. C., "Direct Calculations of Two- and Three-Dimensional Detonations by an Extended CE/SE Method," AIAA Paper 2001-0476, Jan. 2001.

12. He, H., Zhang, Z. C., Yu, S. T. J., and Chang, S. C., "Three-Dimensional Simulations of Detonations by the CE/SE Method Using a Low-Cost Beowulf Cluster," AIAA Paper 2001-0140, Jan. 2001.

13. Tsuboi, N., Katoh, S., and Hayashi, A. K., "Three-Dimensional Numerical Simulation for Hydrogen/Air Detonation: Rectangular and Diagonal Structures," *Proceedings of the Combustion Institute*, Vol. 29, 2002, pp. 2783-2788.

14. Chang, S.-C., "The Method of Space-Time Conservation Element and Solution Element – A New Approach for Solving the Navier-Stokes and Euler Equations," *Journal of Computational Physics*, Vol. 119, 1995, pp.295-324.

15. Chang, S. C., Wang, X. Y., and Chow, C. Y., "The Space-Time Conservation Element and Solution Element Method: A New High-Resolution and Genuinely Multidimensional Paradigm for Solving Conservation Laws," *Journal of Computational Physics*, Vol. 156, 1999, pp. 89-136.

16. Wang, X. Y., and Chang, S. C., "A 2D Non-Splitting Unstructured Triangular Mesh Euler Solver Based on the Space-Time Conservation Element and Solution Element Method," *Computational Fluid Dynamics Journal*, Vol. 8, 1999, pp. 309-325.

17. Zhang, Z.-C., Yu, S.-T. J., and Chang, S.-C., "A Space-Time Conservation Element and Solution Element Method for Solving the Two- and Three-Dimensional Unsteady Euler Equations Using Quadrilateral and Hexahedral Meshes," *Journal of Computational Physics*, Vol. 175, 2002, pp.168-199.

18. Chang, S. C., Himansu, A., Loh, C. Y., Wang, X. Y., and Yu, S. T., "Robust and Simple Non-Reflecting Boundary Conditions for the Euler Equations — A New Approach Based on the Space-Time CE/SE Method," NASA Technical Report TM-2003-212495, 2003.

19. Yu, S. T. and Chang, S. C., "Treatments of Stiff Source Terms in Conservation Laws by the Method of Space-Time Conservation Element and Solution Element," AIAA Paper 97-0435, 1997.

20. White, F. M., *Viscous Fluid Flow*, the 1st edition, McGraw-Hill Book Co., New York, 1974, pp. 195-202.

21. Shuen, S. and Yoon, S., "Numerical Study of Chemically Reacting Flows Using a Lower-Upper Symmetric Successive Overrelaxation Scheme," *AIAA Journal*, Vol. 27, 1989, pp. 1752-1760.

22. Chitsomboon, T., Kumar, A., and Tiwari, S. N., "Numerical Study of Finite-Rate Supersonic Combustion Using Parabolized Equations," AIAA Paper 87-0088, 1987.

23. Shinn, J. L., Yee, H. C., and Uenishi, K., "Extension of a Semi-Implicit Shock Capturing Scheme for Three-Dimensional Fully Coupled Chemically Reactive Flows in Generalized Coordinate Systems," AIAA Paper 87-1577, 1987.

24. Korobeinikov, V. P., Levin, V. A., Markov, V. V., and Chernyi, G. G., "Propagation of Blast Wave in a Combustible Gas," *Astronautica Acta*, Vol. 17 (1972) pp. 529-537.

25. Strehlow, R. A., "Multi-Dimensional Detonation Wave Structure," *Astronautica Acta*, Vol. 15, 1970, pp. 345-357.

26. Guirao, C. M., Knystautas, R., Lee, J. H., Benedick, W. and Berman, M., "Hydrogen-Air Detonations," *Proceedings of the Combustion Institute*, Vol. 19, 1982, pp. 583-590.

27. Kaneshige, M. and Shepherd, J. E., "Detonation database," Technical Report FM97-8, GALCIT, July 1997. See also the electronic hypertext version at http://www.galcit.caltech.edu/detn_db/html/.

28. Erpenbeck, J. J. "Stability of Idealized One-Reaction Detonations," *Physics of Fluids*, Vol. 7, 1964, pp. 684-696.

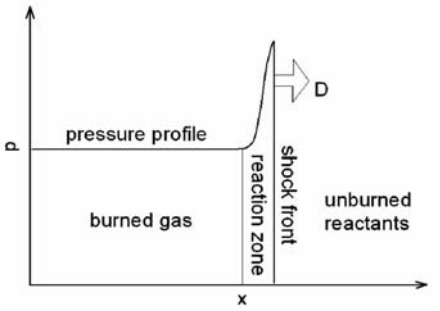

Fig. 1: A schematic of the ZND detonation wave.

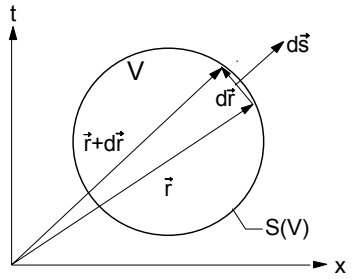

Fig 2: A schematic of space-time integral of the CESE method in one spatial dimension.

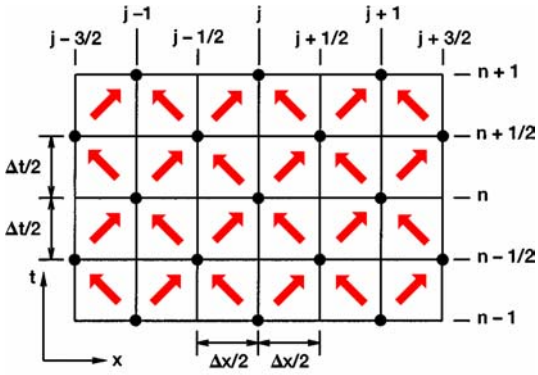

(a)

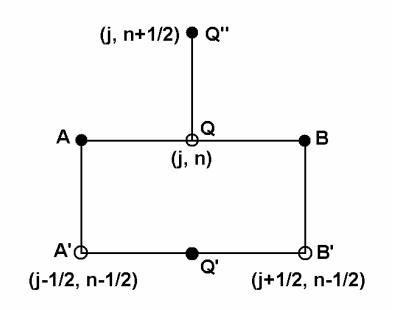

(b)

Fig. 3: Schematics of the CESE method in one spatial dimension: (a) the staggered space-time mesh, (b) SE (j, n) and CE (j, n).

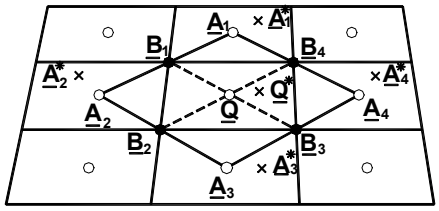

(a)

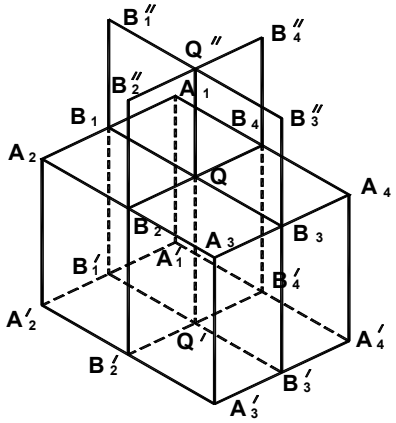

(b)

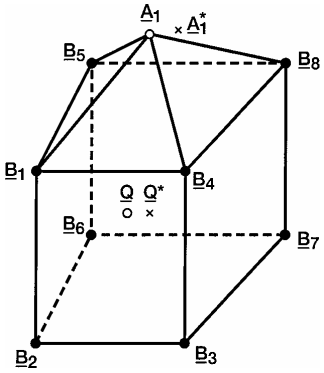

(c)

Fig. 4: The space-time mesh in multi spatial dimensions: (a) 2D grid points in the x-y plane, (b) SE and CE for the 2D scheme, (c) 3D grid points in the x-y-z space.

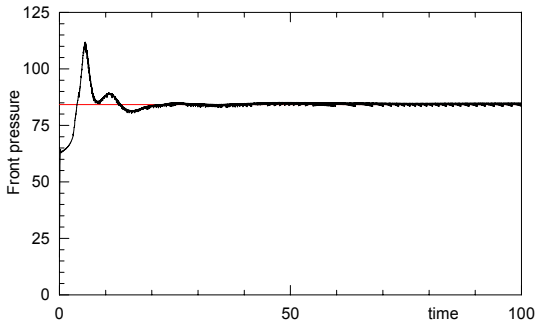

(a)

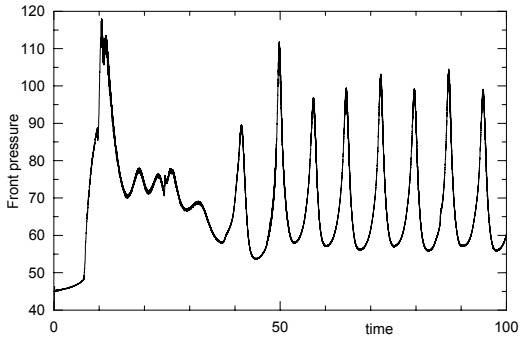

(b)

Fig. 5: Shock front pressure history in the piston problem for (a) $f = 2.0$, (b) $f = 1.6$.

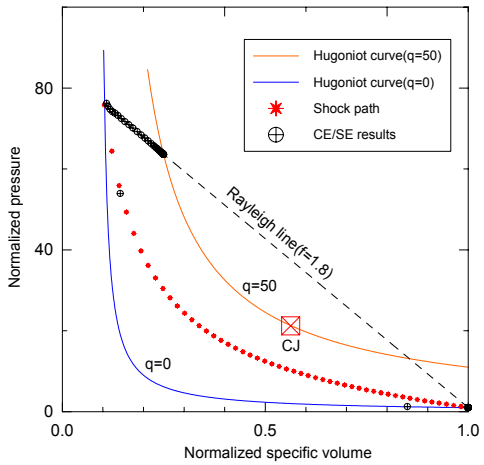

Fig. 6: The p-v diagram of a simulated detonation.

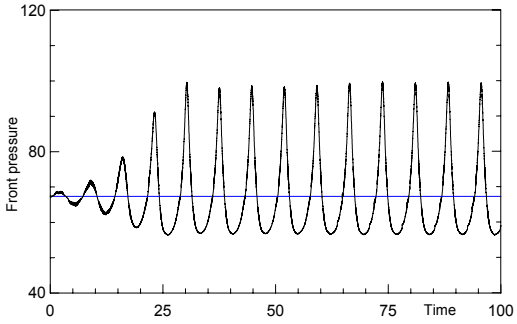

Fig. 7: Time history of the shock pressure for $f = 1.6$ with the resolution of 40 pts/$L_{1/2}$.. The horizontal line is the ZND solution.

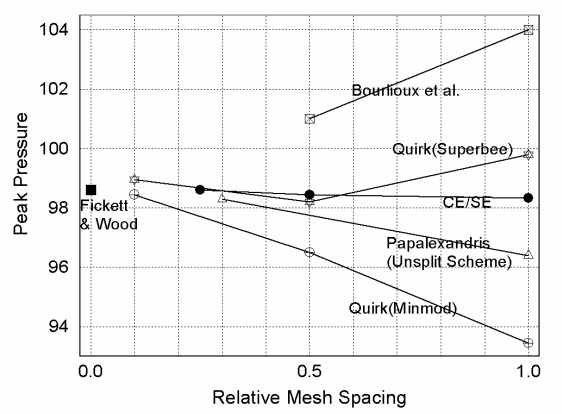

Fig. 8: Variation of peak pressure with grid resolution for various schemes. $f = 1.6$.

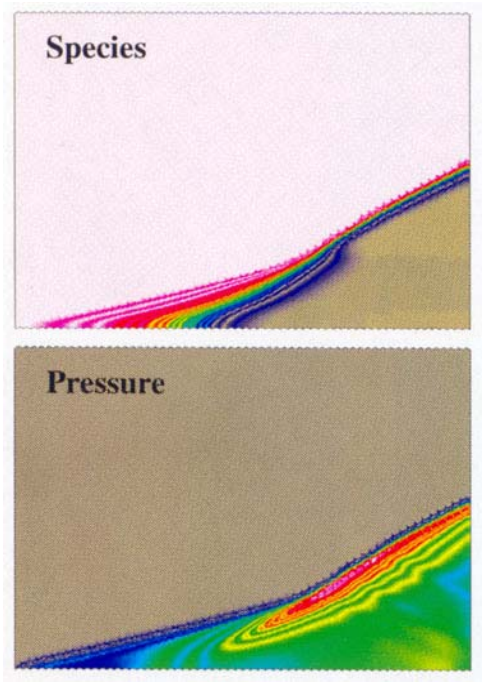

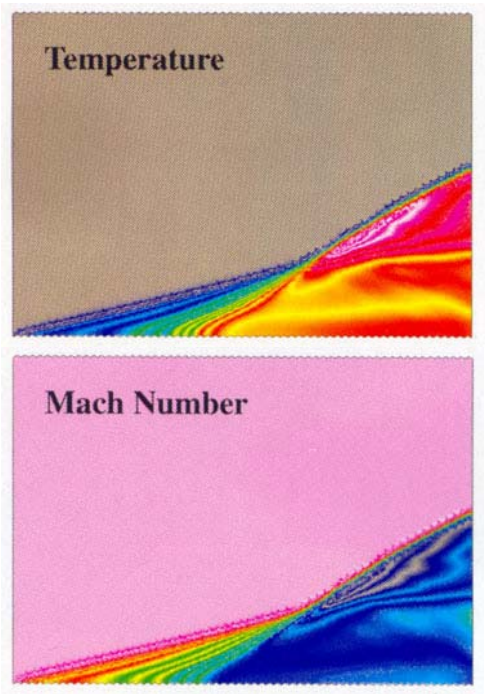

Fig. 9: Shock ignited supersonic combustion with free stream Mach number = 4, temperature = 900 K over a 10 degree ramp.

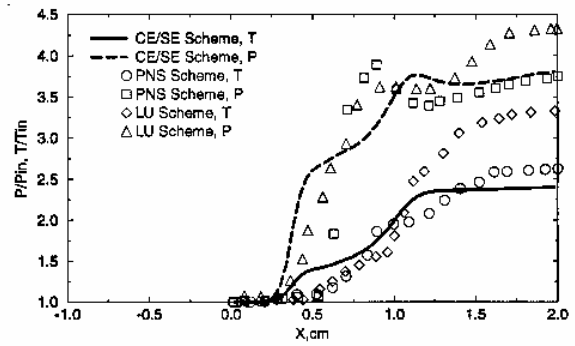

(a)

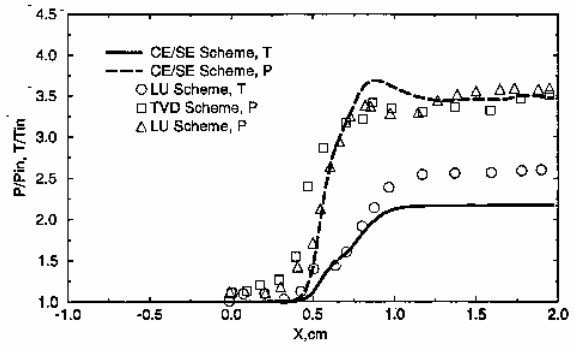

(b)

Fig. 10: The comparison of temperature and pressure between the present calculations and the previous results, including an LU [26], a PNS [27], and a TVD [28] schemes: (a) $T = 900$ K; (b) $T = 1200$ K.

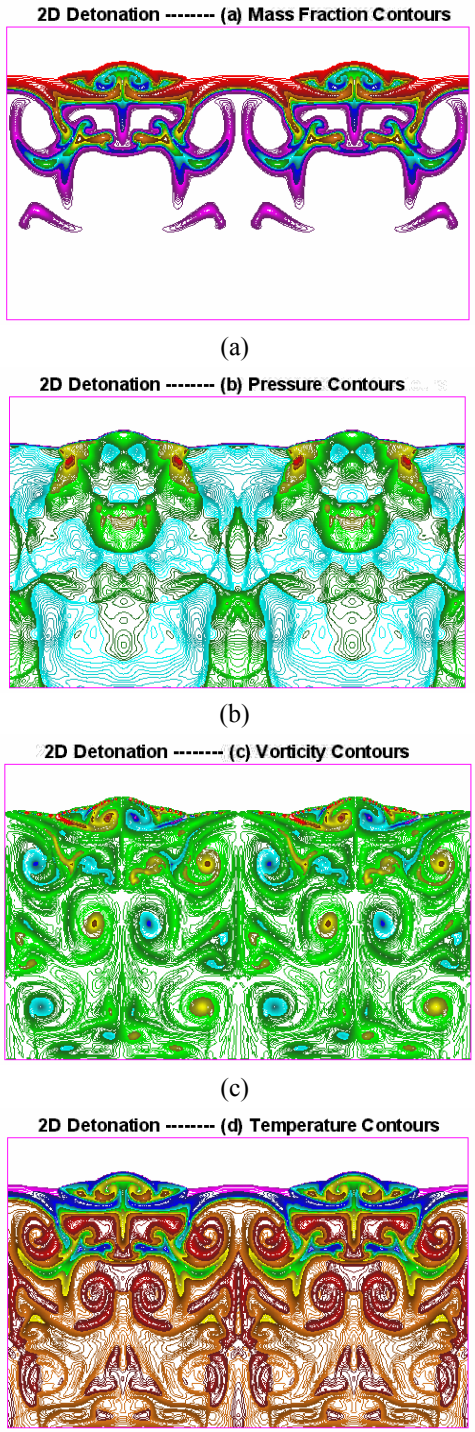

Fig. 11: Two-dimensional detonation waves: (a) mass fraction, (b) pressure, (c) vorticity and (d) temperature.

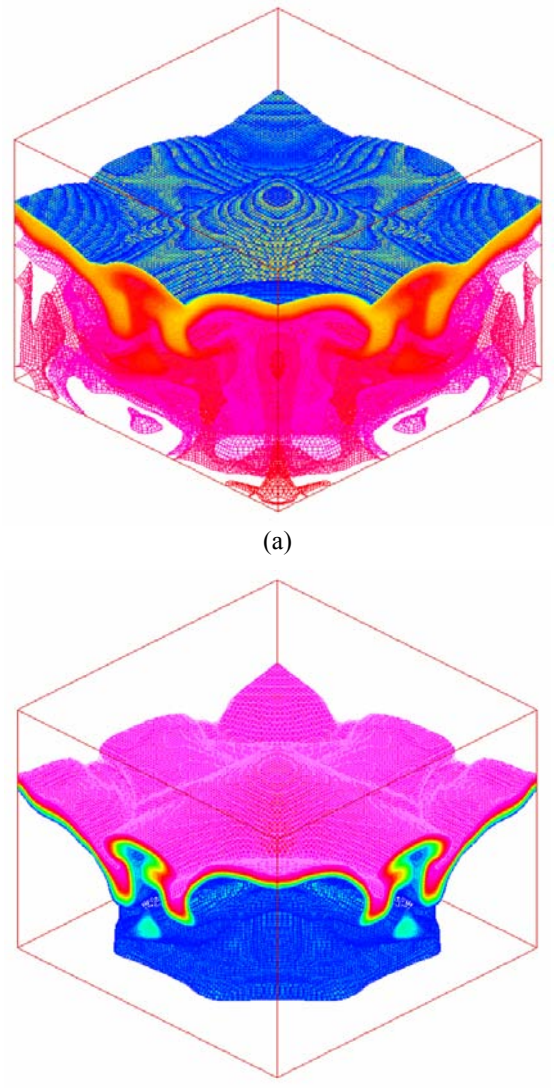

(a)

(b)

Fig. 12: Snapshots of a three-dimensional detonation wave: (a) Temperature contour, (b) Species concentration contour.

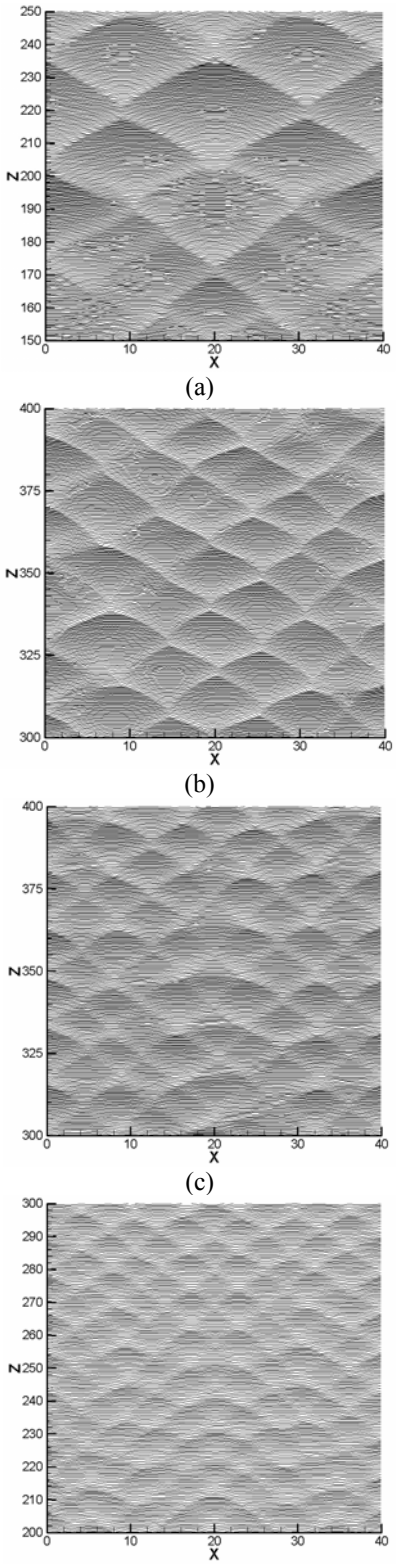

(a)

(b)

(c)

(d)

Fig. 13: Front track on one side wall: $f = 1$, $\gamma = 1.2$, $q_0 = 50$, (a) $E^+ = 20$; (b) $E^+ = 40$; (c) $E^+ = 45$; (d) $E^+ = 50$.

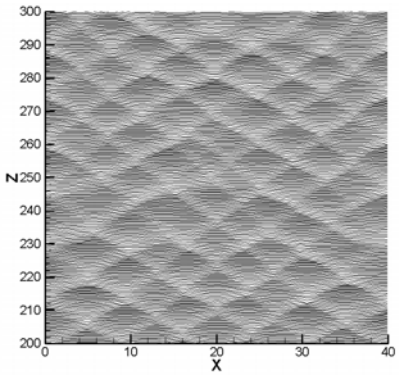

(a)

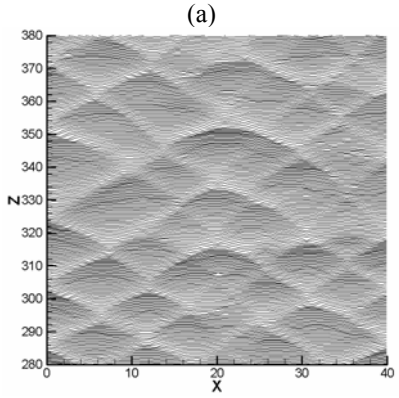

(b)

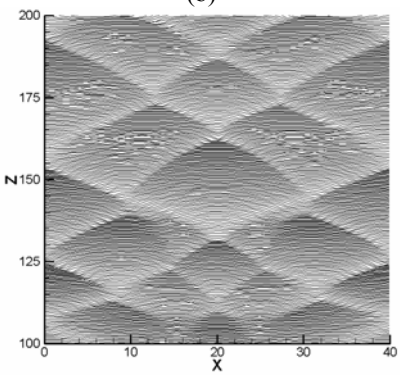

(c)

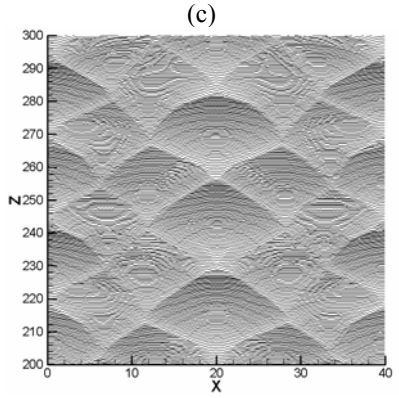

(d)

Fig. 14: Front track on one side wall: $f = 1$, $\gamma = 1.2$, $E^{+} = 35$, (a) $q_0 = 30$; (b) $q_0 = 40$; (c) $q_0 = 50$; (d) $q_0 = 60$.

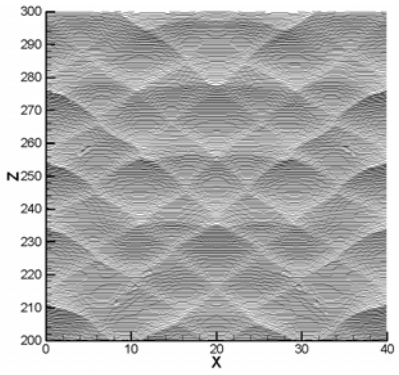

(a)

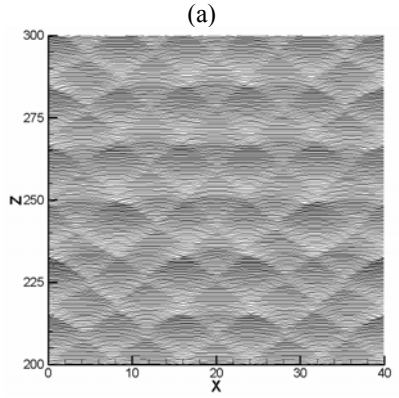

(b)

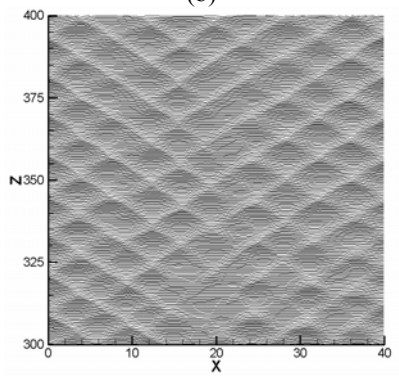

(c)

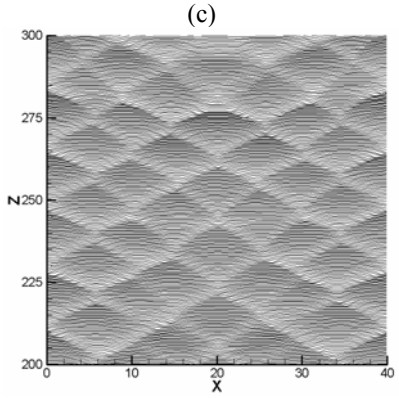

(d)

Fig. 15: Front track on side wall, H_2-Air: (a) $\Phi = 0.7$; (b) $\Phi = 0.8$; (c) $\Phi = 1.0$; (d) $\Phi = 1.4$.

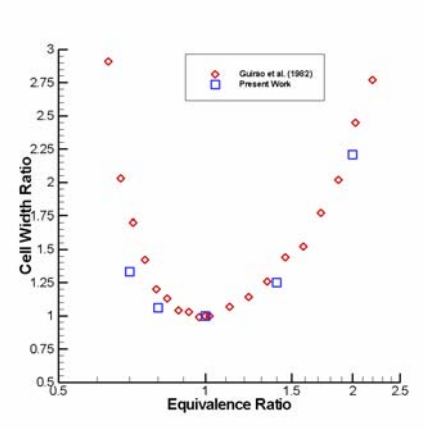

Fig. 16: Cell width versus equivalence ratio for detonations in the H_2-Air mixtures.

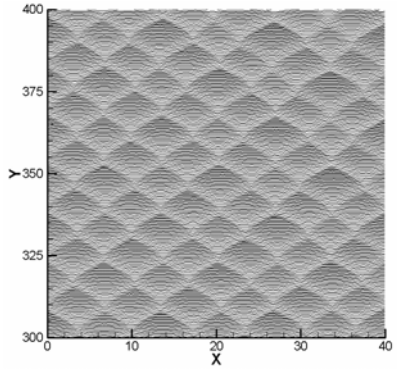

Fig. 17: Front track of the two-dimensional calculations of a detonation propagating in a H_2-Air mixture at Φ = 1.4.

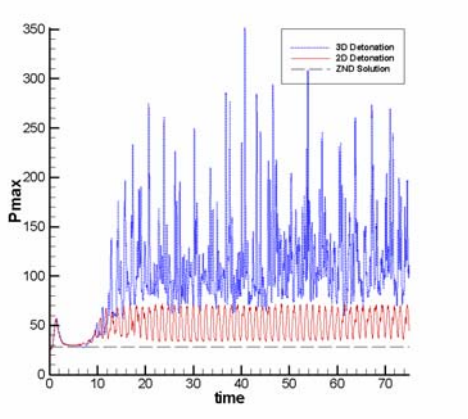

Fig. 18: Time history of the pressure peaks at the shock front for two- and three-dimensional calculations of a CJ detonation wave in a H_2-Air mixture at Φ = 1.4. The results are compared with the ZND analytical solution.

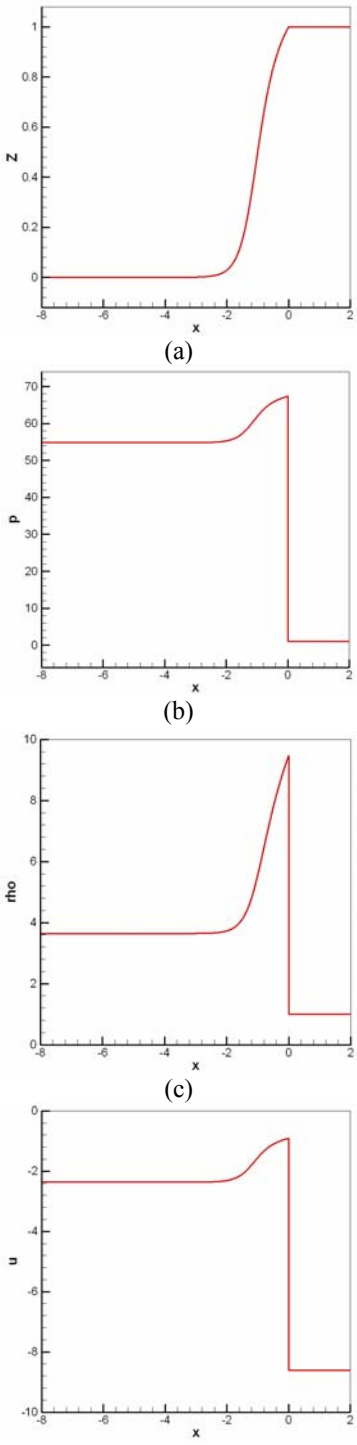

Fig. 19: Flow variable profiles of a one-dimensional ZND detonation wave from the analytical solution: (a) mass fraction of reactant; (b) pressure; (c) density, and (d) velocity. Parameters: γ = 1.2, q_0 = 50, E^+ = 50, and f = 1.6.